Reproduction Analysis of Pile Lateral Loading Experiments using the Distinct Element Method with Focus on Lateral Spreading Pressure

Daisuke Shibata
Japan Port Consultants, Ltd., Japan
daisuke_shibata@jportc.co.jp (corresponding author)

Takashi Nagao
Kobe University, Japan
nagao@people.kobe-u.ac.jp

Received: 12 March 2025 | Revised: 5 April 2025 | Accepted: 9 April 2025

 DOI: https://doi.org/10.48084/etasr.10924

ABSTRACT

During a massive earthquake, large-scale lateral spreading may occur in the ground behind mooring facilities. Regarding structures with pile foundations, such as piers, lateral spreading pressure acts on the piles during lateral spreading formation, while the surrounding soil is displaced through the gaps between the piles. Conventional two-dimensional (2D) analysis methods are generally inadequate for capturing such three-dimensional (3D) effects. The present study employs a 3D Distinct Element Method (DEM) to conduct a reproduction analysis of soil displacement and lateral spreading pressure measured during previous lateral loading experiments. The DEM analysis revealed that, as the load was applied, soil particles moved around the surface of the piles, resulting in an uplift at the front of the pile on the loading side and subsidence at the back of the pile. These results closely corresponded to the observed movement of soil particles during the experiments. Due to the differences in the contact conditions between the pile and the surrounding soil before loading, the lateral spreading pressure acting on the lower part of the pile was found to be higher in the analytical results than in the experimental ones. However, the analytical results agreed with the experimental data in terms of the lateral spreading pressure acting on the upper part of the pile.

Keywords-pile; lateral spreading pressure; distinct element method

I. INTRODUCTION

Mooring facilities are critical components of port infrastructure, primarily used for cargo handling operations. They are usually built on soft and weak soils found in coastal regions. During seismic events, these structures are affected not only by inertial forces, but also by increased earth pressure and potential soil liquefaction beneath the surface. As a result, the structures may undergo lateral displacement toward the sea, leading to potential damage [1–5]. During massive earthquakes, large-scale lateral spreading is often induced. For instance, during the Hyogoken-Nanbu Earthquake in 1995, many port structures were subjected to damage, with the caisson quay walls at Kobe Port being displaced several meters toward the sea. At the Takahama Pier in Kobe Port, buckling occurred at both the pile head and the pile's embedded section. The buckling of the embedded portion of the pile was attributed to lateral spreading pressure acting on the pier piles as the ground behind the pier moved laterally toward the sea, causing the lateral spreading pressure to be transmitted from the underlying rubble layers beneath the pier [1]. Therefore, when large seismic motions are anticipated and when there is a possibility that mooring facilities may be subjected to the effects of lateral spreading, it is critical to adequately assess the safety of structures under lateral spreading pressure.

In pier structures supported by piles, mass is concentrated in the superstructure. Consequently, the simplified design methods [1, 6] employed in the seismic design practice of such piers only consider the inertial forces acting on the superstructure; lateral spreading pressure is typically not considered. One approach for evaluating pile safety under the influence of lateral spreading pressure is the application of the beam on the Winkler foundation model. This model represents the pile as a beam and the soil as a spring. However, during major seismic events, the soil exhibits nonlinear behavior, necessitating the modeling of the spring as a nonlinear type. Despite this, there is limited research on specific methods for setting the nonlinear characteristics of the spring. The maximum spring force is generally taken as the passive earth pressure based on the design method for a continuous wall. However, according to a lateral loading experiment that measured the lateral spreading pressure acting on piles [7], the

maximum lateral spreading pressure was greater than the passive earth pressure. This depends on the difference between continuous walls and discretely installed piles. Nevertheless, there is a lack of knowledge regarding the appropriate method for setting the upper limit of lateral spreading pressure acting on piles.

Another method for evaluating the impact of lateral spreading pressure on piles is the Finite Element Analysis (FEA), which models both the soil and the structure. From the perspective of reducing computational load, 2D analyses are commonly applied. Previous studies have assessed the seismic performance of mooring facilities, such as sheet-pile-type quay walls and piers with pile foundations [8-13]. In these analyses, piles are typically modeled as beam elements, and either adjacent soil elements share nodes with the piles or joint elements are placed between the piles and the soil to represent sliding in the axial direction and separation in the perpendicular direction. During lateral spreading, the soil flows through the gaps between the discretely installed piles. This phenomenon, though, cannot be accurately captured through these methods, leaving unresolved issues in the precise evaluation of the lateral spreading pressure acting on the piles. To address this, some cases in the FEA code FLIP model the interaction between the piles and the soil by introducing pile-soil interaction spring elements [14, 15]. However, it has been pointed out that 2D analyses cannot reproduce 3D effects [16], creating a limitation in accurately capturing the full behavior of lateral spreading pressure. The 3D DEM [17] is another method for assessing the lateral spreading pressure acting on piles. DEM has been widely deployed in civil engineering, with numerous successful applications being observed in slope failure analysis and seabed scour analysis in offshore wind turbine foundations [18-23]. Additionally, significant research has been conducted on the vertical bearing capacity of piles and their lateral resistance [24-28]. However, no existing studies have used 3D DEM to evaluate the lateral spreading pressure acting on piles. Thus, the current research aims to analytically assess the lateral spreading pressure acting on piles by reproducing the results of previous lateral loading experiments [7] using 3D DEM.

II. METHOD

A. Overview of Previous Lateral Loading Experiment [7]

Regarding the lateral loading experiment setup, a soil tank with dimensions of 500 mm in width, 500 mm in depth, and 500 mm in height was used. A model pile with a diameter of 60 mm and a length of 200 mm was fixed to the bottom plate of the tank with a pile spacing of 220 mm. The pile arrangement was set based on the foundation of the pier. It should be noted that this corresponds to a single pile condition, and that the response may be different in the group pile condition. The soil used was Tohoku Silica Sand No. 6 in the dry state, which was air-pluviated to achieve a relative density of approximately 75%, and then filled to a height of 100 mm. The soil tank side frame was independently loaded horizontally by a mega torque motor, which applied horizontal displacement to the soil and induced lateral spreading pressure on the model piles. The length scaling factor was set to λ = 1/100 (model/prototype). The similitude proposed in [31] was applied. To perform measurements, soil pressure gauges were mounted using fitting jigs at two heights on the model pile—50 mm and 75 mm above its bottom plate. These gauges were placed in the direction of the loading plate (hereafter referred to as the pile front) to measure the lateral spreading pressure. Other measurement items included the horizontal displacement of the soil tank frame, applied load, and surface displacement of the soil. As the loading increased, the readings of the soil pressure gauges increased to a certain limit after which they began to decrease. The surface of the soil exhibited an uplift on the pile front and a hollow on the back pile.

B. Analytical Method Using Distinct Element Method

In the 3D DEM, the soil and structure are modeled using rigid particles, with the intervals of the particles being connected by springs and dashpots. The linearity and nonlinearity of the material properties of the soil and structure are represented through the characteristics of the springs and dashpots. The equations of motion for any given element are:

$$F = m\ddot{x} + c\dot{x} \quad (1)$$

$$M = I\ddot{\varphi} + cr^2\dot{\varphi} \quad (2)$$

$$c = 2h\sqrt{mk} \quad (3)$$

where F is the resultant force acting on the element, m is the mass of the element, $\ddot{x}$ is the acceleration of the element, c is the viscosity coefficient, $\dot{x}$ is the velocity, M is the bending moment acting on the element, I is the moment of inertia of the element, $\ddot{\varphi}$ is the angular acceleration of the element, r is the radius, $\dot{\varphi}$ is the angular velocity, h is the damping constant, and k is the spring constant. F and M represent the sum of the external forces and moments transmitted between elements connected by four types of springs: axial spring, shear spring, rotational spring, and torsional spring, as displayed in Figure 1. Dashpots are connected in parallel with all four types of springs. When a spring consistently reaches its pre-failure strength, it is considered to have failed and is subsequently replaced by a spring with post-failure strength. The force acting on each element at the current time step is calculated based on its position in the previous time step. From there, the acceleration is calculated using the equation of motion, and numerical integration is utilized to obtain the velocity and displacement. For any two elements I, J with coordinates $I(x_i, y_i, z_i)$, $J(x_j, y_j, z_j)$, and radii r_i, r_j the contact determination between elements I and J at time t is expressed by:

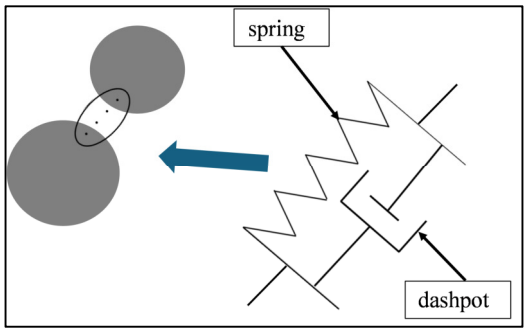

Fig. 1. Element model applied to DEM.

$$r_i + r_j \geqq R_{ij} \tag{4}$$

where:

$$R_{ij} = \sqrt{\left(x_j - x_i\right)^2 + \left(y_j - y_i\right)^2 + \left(z_j - z_i\right)^2} \tag{5}$$

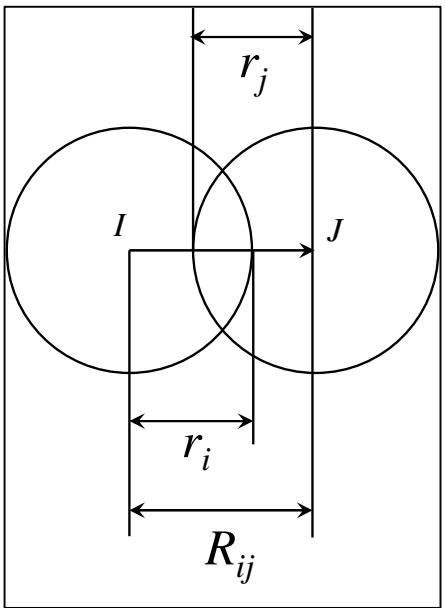

Fig. 2. Contact determination of elements.

For all elements J that come into contact with element I, the vectors $\left[\overrightarrow{f_n}\right]_t$, $\left[\overrightarrow{f_s}\right]_t$, $\left[\overrightarrow{p_{fn}}\right]_t$, and $\left[\overrightarrow{p_{fs}}\right]_t$ are calculated, and the resultant forces are then determined. The total force vector $\overrightarrow{|F_i|}_t$ acting on element I at time t is given by:

$$\overrightarrow{|F_i|}_t = \Sigma\left\{\left[\overrightarrow{f_n}\right]_t + \left[\overrightarrow{f_s}\right]_t + \left[\overrightarrow{p_{fn}}\right]_t + \left[\overrightarrow{p_{fs}}\right]_t\right\} \tag{6}$$

The total moment vector $\overrightarrow{|F_{mi}|}_t$ acting on element I at time t is expressed as:

$$\overrightarrow{|F_{mi}|}_t = \left\{r_i/\left|\vec{I}_j\right|\right\} \cdot \vec{I}_j \times \left[\overrightarrow{f_s}\right]_t + \vec{I}_j \times \left[\overrightarrow{p_{fs}}\right]_t \tag{7}$$

The acceleration at time t is expressed as:

$$\left[\overrightarrow{\ddot{u}_i}\right]_t = \left[\vec{f}_i\right]_t / m_i \tag{8}$$

$$\left[\overrightarrow{\ddot{\Phi}_i}\right]_t = \left[\overrightarrow{f_{mi}}\right]_t / I_i \tag{9}$$

where $\left[\overrightarrow{u_i}\right]_t = \left(u_{xi},\, u_{yi},\, u_{zi}\right)$ is the position vector of element I at time t, $\left[\overrightarrow{\varphi_i}\right]_t = \left(\varphi_{xi},\, \varphi_{yi},\, \varphi_{zi}\right)$ is the rotation vector of element I at time t, m_i is mass of element I, and I_i is the moment of inertia of element I. The velocity at time t can be obtained by integrating the acceleration computed from using the above equations. The density ρ and volume V (calculated by (10)) are also considered in the calculation. Since a 3D analysis is used in this study, the mass m_i and the moment of inertia I_i can be expressed by (11) and (12). Additionally, by integrating the accelerations obtained from (8) and (9), the velocity at time t can be determined as in (13) and (14):

$$V = \frac{4}{3}\pi {r_i}^3 \tag{10}$$

$$m_i = \rho V \tag{11}$$

$$I_i = \frac{2}{5} m_i {r_i}^2 \tag{12}$$

$$\left[\overrightarrow{\dot{u}_i}\right]_t = \left[\overrightarrow{\dot{u}_i}\right]_{t-\Delta t} + \left[\overrightarrow{\ddot{u}_i}\right]_t \Delta t \tag{13}$$

$$\left[\overrightarrow{\dot{\Phi}_i}\right]_t = \left[\overrightarrow{\dot{\Phi}_i}\right]_{t-\Delta t} + \left[\overrightarrow{\ddot{\Phi}_i}\right]_t \Delta t \tag{14}$$

By integrating the above, the change in position and rotation is given by:

$$\left[\overrightarrow{\Delta u_i}\right]_t = \frac{1}{2} \cdot \left\{\left[\overrightarrow{\dot{u}_i}\right]_t + \left[\overrightarrow{\dot{u}_i}\right]_{t-\Delta t}\right\} \cdot \Delta t \tag{15}$$

$$\left[\overrightarrow{\Delta \Phi_i}\right]_t = \frac{1}{2} \cdot \left\{\left[\overrightarrow{\dot{\Phi}_i}\right]_t + \left[\overrightarrow{\dot{\Phi}_i}\right]_{t-\Delta t}\right\} \cdot \Delta t \tag{16}$$

Thus, the position of the element at time t is expressed as:

$$\left[\overrightarrow{u_i}\right]_t = \left[\overrightarrow{\Delta u_i}\right]_t + \left[\overrightarrow{u_i}\right]_{t-\Delta t} \tag{17}$$

$$\left[\overrightarrow{\Phi_i}\right]_t = \left[\overrightarrow{\Delta \Phi_i}\right]_t + \left[\overrightarrow{\Phi_i}\right]_{t-\Delta t} \tag{18}$$

Using the positions of the elements at time t, the resultant force, acceleration, velocity, and displacement acting on the element at time $t + \Delta t$ can be calculated. The springs used to calculate the total force and moment on the elements are expressed as:

1. Spring for element I

$$k_{Axiali} = \frac{E_i A_i}{r_i},\ k_{Sheari} = \frac{G_i A_i}{r_i},\ k_{Torsioni} = \frac{G_i I_{ti}}{r_i},$$

$$k_{Bendingi} = \frac{E_i I_i}{r_i} \tag{19}$$

2. Spring for element J

$$k_{Axialj} = \frac{E_j A_j}{r_j},\ k_{Shearj} = \frac{G_j A_j}{r_j},\ k_{Torsionj} = \frac{G_j I_{tj}}{r r_j},$$

$$k_{Bendingj} = \frac{E_j I_j}{r_j} \tag{20}$$

where A is the contact cross-sectional area, I is the moment of inertia, and I_t is the second polar moment of area.

Since the two springs are connected in series, the spring constants between elements are expressed as:

$$\frac{i}{k_{Axial}} = \frac{i}{k_{Axiali}} + \frac{i}{k_{Axialj}} \tag{21}$$

$$\frac{i}{k_{Shear}} = \frac{i}{k_{Sheari}} + \frac{i}{k_{Shearj}} \tag{22}$$

$$\frac{i}{k_{Torsion}} = \frac{i}{k_{Torsioni}} + \frac{i}{k_{Torsionj}} \tag{23}$$

$$\frac{i}{k_{Bending}} = \frac{i}{k_{Bendingi}} + \frac{i}{k_{Bendingj}} \tag{24}$$

where four types of spring constants are expressed as:

$$k_{Axial} = \frac{1}{\frac{1}{k_i} + \frac{1}{k_j}} = \frac{1}{\frac{1}{E \cdot \pi \cdot R_i \cdot {Ap_i}^2} + \frac{1}{E \cdot \pi \cdot R_j \cdot {Ap_j}^2}} \tag{25}$$

$$k_{Shear} = \frac{1}{\frac{1}{k_i}+\frac{1}{k_j}} = \frac{1}{\frac{1}{G\cdot\pi\cdot R_i\cdot {Sp_i}^2}+\frac{1}{G\cdot\pi\cdot R_j\cdot {Sp_j}^2}} \quad (26)$$

$$k_{Torsion} = \frac{1}{\frac{1}{k_i}+\frac{1}{k_j}} = \frac{1}{\frac{2}{G\cdot\pi\cdot {R_i}^3\cdot {Tp_i}^4}+\frac{2}{G\cdot\pi\cdot {R_j}^3\cdot {Tp_j}^4}} \quad (27)$$

$$k_{Bending} = \frac{1}{\frac{1}{k_i}+\frac{1}{k_j}} = \frac{1}{\frac{4}{E\cdot\pi\cdot {R_i}^3\cdot {Bp_i}^4}+\frac{4}{E\cdot\pi\cdot {R_j}^3\cdot {Bp_j}^4}} \quad (28)$$

where k_{Axial} is the axial spring coefficient, k_{Shear} is the shear spring coefficient, $k_{Torsion}$ is the torsional spring coefficient, $k_{Bending}$ is the bending spring coefficient, E is Young's modulus, G is the shear modulus, Ap_i is the axial index of particle I, Ap_j is the axial index of particle J, Sp_i is the shear index of particle I, Sp_j is the shear index of particle J, Tp_i is the torsional index of particle I, Tp_j is the torsional index of particle J, Bp_i is the bending index of particle I, and Bp_j is the bending index of particle J. In addition, the axial, shear, bending, and torsional indices are values related to the contact width when determining the spring constants, and they are expressed as the ratio of the contact width to the section width. The 3D DEM analysis model is illustrated in Figure 3. Generally, the time step Δt is expressed as a relationship between the mass of the particle m and the spring constant k:

$$\Delta t \propto \sqrt{m/k} \quad (29)$$

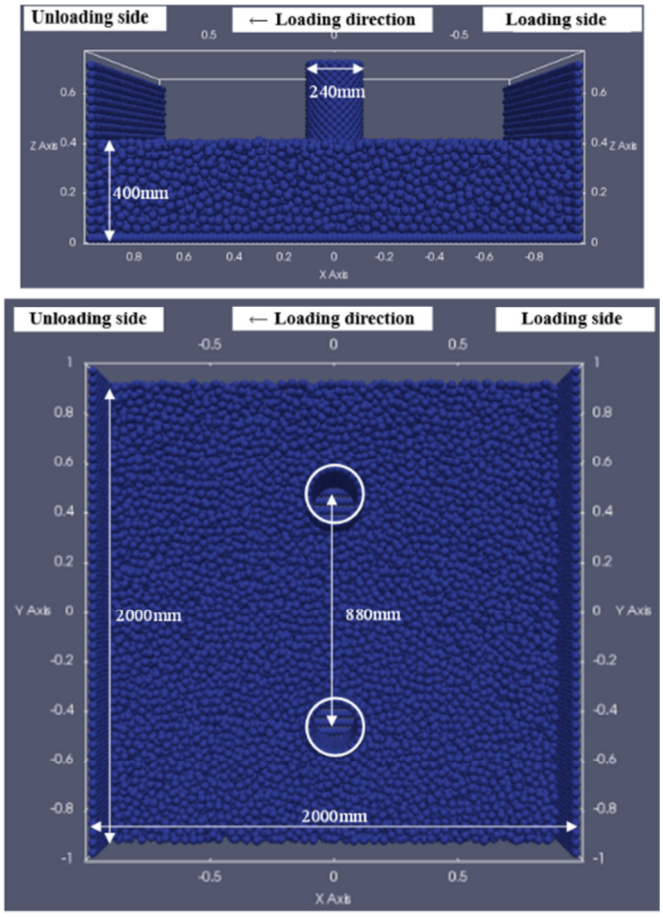

Fig. 3. Analysis model.

Analysis accuracy depends on the time step, and as the particle diameter decreases, it is necessary to reduce the time step for the analysis to be accurate [32]. Furthermore, reducing the used particle diameter increases the number of particles in the model, thereby increasing the computational load. In this study, to reduce the computational load while maintaining analysis accuracy, the scale of the soil tank and piles was set to four times that of the experiment, the particle radius was set to 0.02 m, and the time step for the analysis was set to 5×10^{-7} s. The dimensions of the bottom plate are 2000 mm in width and 2000 mm in length. Two piles (with a diameter of 240 mm and length of 700 mm) were arranged on the bottom plate such that they did not interfere with the particles constituting the bottom plate. Since the piles were modeled as rigid bodies, the coordinates of the constituent particles were fixed. By applying a forced displacement to the loading plate integrated with the bottom plate, horizontal displacement was imparted to the soil particles. The ground was created using self-weight analysis, simulating an air pluviation method, with a layer thickness of 400 mm. The loading speed of the loading plate was set at 0.018 m/s, based on [33], with a loading time of 10 s.

The analysis parameters are presented in Table I. If the axial, shear, bending, or torsional indices are set too high, the maximum overlap of particles may increase, leading to a significant decrease in the soil particle volume during loading. Therefore, these indices were set to relatively small values of 0.1. The density ρ was taken as 2.65 t/m³, corresponding to the typical density of No.6 silica sand.

TABLE I. ANALYSIS PARAMETERS

Material name	Unit	Pile	Sand	Loading plate
Particle radius	m	0.01	0.02	0.02
Axial index	—	0.1	0.1	0.1
Shear index	—	0.1	0.1	0.1
Torsional index	—	0.1	0.1	0.1
Bending index	—	0.1	0.1	0.1
Density	g/cm^3	2.65	2.65	2.65
Young's modulus	kN/m^2	80000000	20000000	20000000
Shear modulus	kN/m^2	30000000	7500000	7500000
Damping constant	—	0.5	0.5	0.5
Compressive strength (before failure)	kN/m^2	92000	400000	400000
Tensile strength (before failure)	kN/m^2	0.1	40000	400000
Cohesion (before failure)	kN/m^2	0.1	40000	400000
Friction coefficient (before failure)	—	0.5	0.5	0.5
Compressive strength (after failure)	kN/m^2	92000	400000	400000
Tensile strength (after failure)	kN/m^2	0.1	40000	400000
Shear strength (after failure)	kN/m^2	0.1	40000	400000
Friction coefficient(after failure)	—	0.5	0.5	0.5
Time step for analysis	s	0.0000005		

The Young's modulus E was set to 8×10^6 kN/m^2, a typical value for sand particles, and the shear modulus G was set to 3×10^6 kN/m^2, which is calculated from (30) using a Poisson's ratio of 0.3. The compressive strength was set to 92000 kPa, a typical value for sand particles. Since the compressive strength of sand particles does not change before and after loading, the same value was used for both the pre-failure and post-failure states of the particle bonds. The total number of particles utilized in the analysis was 29603, comprising 3040 pile particles, 6930 loading wall and bottom plate particles, and 19633 soil particles.

$$G = \frac{E}{2(1+\nu)} \quad (30)$$

III. RESULTS AND DISCUSSION

A. Displacement of Sand Particles

Figures 4-6 illustrate the displacement contours of sand particles at the ground surface under a displacement of 15 mm. In the X direction, corresponding to the movement of the loading plate, the displacement values at the back of the loading plate, the front of the unloading plate, and between the piles are approximately the same, indicating that sand particles flow effectively through the space between the piles. Conversely, in the areas in front of and behind the piles, the displacement of the sand particles is minimal, suggesting that the piles obstruct the movement of the sand particles. In the Y direction, perpendicular to the loading plate's movement, significant displacements are observed primarily in the vicinity of the piles. In front of the piles, sand particles appear to move around the piles, migrating toward the back surface of the pile. In contrast, on the back surface of the piles, sand particles move toward the Y coordinate of the pile center. This displacement is not caused by the compression of the sand particles that have turned around from the front of the pile; instead, it is attributed to the formation of a hollow on the back of the piles due to loading, causing sand particles to settle toward the Y coordinate of the pile center. In the vertical (Z) direction, prominent displacements are again primarily observed around the piles. Sand particles in front of the piles are displaced upward, while those behind the piles experience subsidence. These displacement patterns align well with the experimental observations, validating that DEM accurately reproduces the movement of the sand particles.

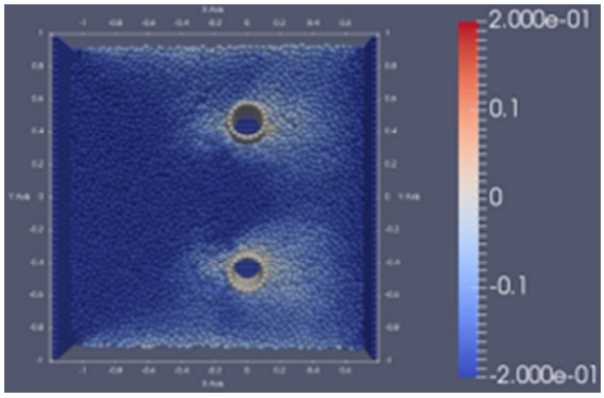

Fig. 4. X-direction displacement contour (unit: m) (blue (-): move to the left, red (+): move to the right).

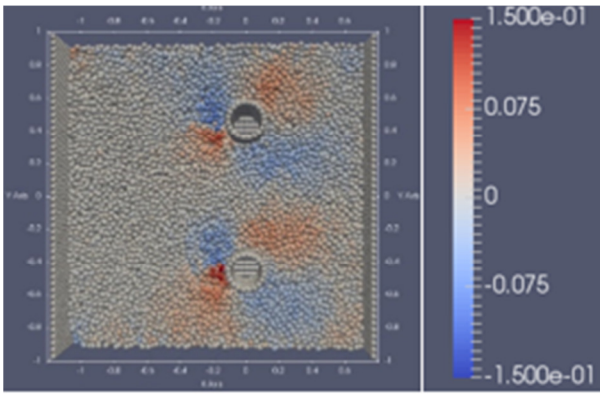

Fig. 5. Y-direction displacement contour (unit: m) (blue (-): move down, red (+): move up).

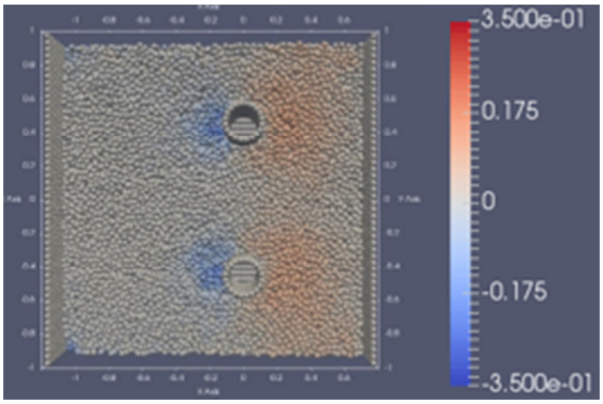

Fig. 6. Z-direction displacement contour (unit: m) (blue (-): subsidence, red (+): heave).

B. Lateral Spreading Pressure

Figures 7 and 8 demonstrate a comparison between the analytical results and the experimental data for the lateral spreading pressure acting on the piles. The lateral spreading pressure in the analysis was determined by averaging the contact forces between the pile particles and the soil particles at a height corresponding to the center of the soil pressure gauges used in the model experiment. This average contact force was then divided by the cross-sectional area of the soil particles to convert it into pressure. At the lower installation height of the soil pressure gauge, the effective confining pressure is greater, leading to a higher lateral spreading pressure compared to the upper gauge. This observation is consistent with previous models' experimental results. Overall, the lateral spreading pressure obtained from the analysis closely matches the experimental data, although the values recorded at the upper gauge are slightly lower than those measured in the experiments. In the experimental setup, the soil density was 1.52 t/m³, whereas in the analytical model, the particle diameter was 4 cm, larger than that used in the experiments. This led to a larger void between particles and a smaller soil density (1.14 t/m³) in the analysis. Consequently, the effective overburden pressure of the near-surface region was lower in the analysis compared to the experiment, resulting in a smaller applied pressure. Conversely, the analysis values at the lower pressure gauge were larger than the experimental values. There was a

significant difference between the two values immediately after loading. In the analysis, right after loading began, the value increased rapidly because the ground in front of the pile was compressed without significant movement of the sand particles being observed. In contrast, during the experiment, the lateral spreading pressure increased gradually as the loading progressed. This difference arises from the variation in the contact conditions between the sand particles and the pile before loading at the locations where the earth pressure gauges were installed in both the experiment and the analysis. Previous loading experiments and reproduction analyses of piles focused on the small displacement range in the initial loading stage [34]. In contrast, this study successfully reproduced the lateral spreading pressure in the large soil displacement range.

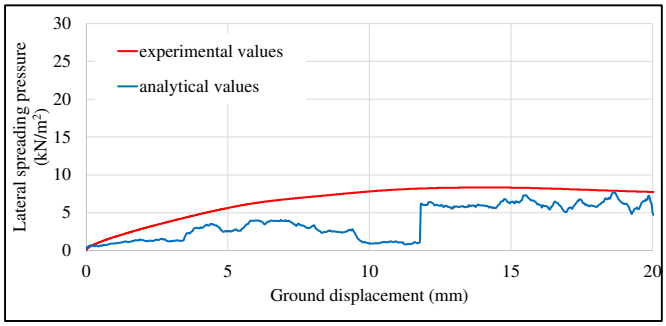

Fig. 7. Comparison between the analytical values and the experimental values (upper gauge).

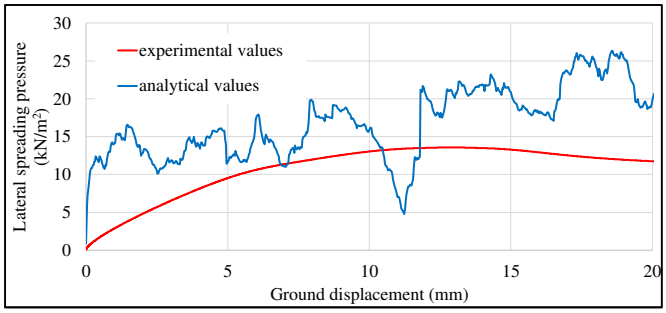

Fig. 8. Comparison of analytical and experimental lateral spreading pressure values at the lower soil pressure gauge.

Figures 9 and 10 show the X-component of the composite displacement vector (comprising X, Y, and Z components). Here, the solid white line represents the pile. The region where the displacement in the X-direction is small around the pile surface (enclosed by the white dashed line) is wider in the upper gauge than in the lower gauge. At the upper gauge, the lower confining pressure allows soil particles to move more freely around the pile during lateral spreading. Consequently, the displacement in the X-direction on the front surface of the pile is smaller than the overall lateral spreading. Lateral spreading pressure can be calculated by multiplying the lateral spreading quantity by the subgrade reaction modulus, which is evaluated based on the ground deformation modulus. It is known that the ground deformation modulus depends on the confining pressure, which is proportional to the overburden pressure. The shear modulus of the ground is proportional to the square root of the confining pressure [35], and Young's modulus is proportional to the shear modulus, as given by (28). Therefore, it can be assumed that the subgrade reaction modulus increases with depth, proportional to the square root of the depth. Based on this, if the lateral spreading quantity remains constant with depth, the lateral spreading pressure will also increase with depth, proportional to the square root of the depth. However, particularly in the analysis results, the lateral spreading pressure in the lower gauge is significantly larger than the upper gauge. This suggests that the lateral spreading quantity is not constant concerning depth.

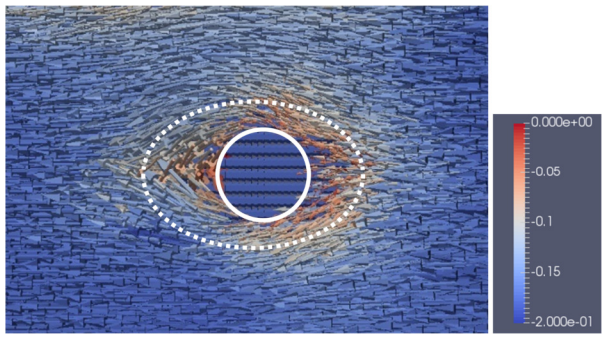

Fig. 9. Composite displacement vector (X- component) (unit: m) (upper section).

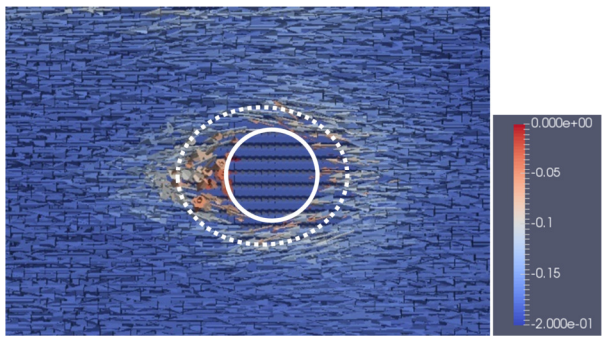

Fig. 10. Composite displacement vector (X-component) (unit: m) (lower section).

IV. CONCLUSIONS

This study aims to quantitatively assess the lateral spreading pressure acting on a pile when the surrounding ground is displaced through the gaps between piles. To achieve this, the results of previous horizontal loading experiments were reproduced using a three-dimensional (3D) Distinct Element Method (DEM). The main conclusions drawn are:

- In the DEM analysis of soil particle movement at the ground surface, soil particles slipped between the piles with loading, while at the front and back of the pile, the pile acted as an obstacle, resulting in only minimal soil particle movement. In the direction perpendicular to the loading plate's movement, soil particles at the front of the pile moved around the pile towards its the back side, while at the back of the pile, a hollow formed, causing movement towards the pile's center. In the vertical direction, soil particles at the front of the pile rose, and sank at its back

part. The patterns of these soil particle displacements are consistent with previous experimental results, confirming that DEM successfully reproduced the movement of the sand particles.

- The lateral spreading pressure at the lower gauge was higher than at the upper gauge, consistent with previous experimental results. At the upper gauge, the analytical pressure was slightly lower than its experimental value, primarily due to the lower soil density used in the analysis. Conversely, the analytical pressure at the lower gauge was higher than in the experiment, with a notable spike being noted immediately after loading. This discrepancy is attributed to the differing pre-loading contact conditions between soil particles and the pile at the gauge locations. Unlike previous studies, this analysis successfully captured the behavior of lateral spreading pressure under large soil displacements.
- When comparing the lateral spreading quantity at the front of the pile, the result showed that it was smaller in the upper gauge and larger in the lower gauge. This is because the ease with which soil particles move around the pile is dependent on the confining pressure. The significant difference in the lateral spreading pressure analysis values between the upper and lower gauges is primarily influenced by the difference in lateral spreading quantities.

ACKNOWLEDGMENT

Masayuki Yamada provided the DEM program used in this study. Masahide Otsubo and Shunpei Matsuo offered valuable advice during this research.

REFERENCES

[1] *Seismic Design Guidelines for Port Structures. Japan: International Navigation Association, 2001.*

[2] G. Mondal and D. C. Rai, "Performance of harbour structures in Andaman Islands during 2004 Sumatra earthquake," *Engineering Structures*, vol. 30, no. 1, pp. 174–182, Jan. 2008, https://doi.org/10.1016/j.engstruct.2007.03.015.

[3] R. A. Green *et al.*, "Geotechnical Aspects of Failures at Port-au-Prince Seaport during the 12 January 2010 Haiti Earthquake," *Earthquake Spectra*, vol. 27, no. 1_suppl1, pp. 43–65, Oct. 2011, https://doi.org/10.1193/1.3636440.

[4] S. Werner *et al.*, "Seismic Performance of Port de Port-au-Prince during the Haiti Earthquake and Post-Earthquake Restoration of Cargo Throughput," *Earthquake Spectra*, vol. 27, no. 1_suppl1, pp. 387–410, Oct. 2011, https://doi.org/10.1193/1.3638716.

[5] T. Sugano, A. Nozu, E. Kohama, K. Shimosako, and Y. Kikuchi, "Damage to coastal structures," *Soils and Foundations*, vol. 54, no. 4, pp. 883–901, Aug. 2014, https://doi.org/10.1016/j.sandf.2014.06.018.

[6] *Technical Standards and Commentaries for Port and Harbour Facilities in Japan. National Institute for Land and Infrastructure Management Port Facilities Division, 2022.*

[7] T. Nagao and D. Shibata, "Experimental Study of the Lateral Spreading Pressure Acting on a Pile Foundation During Earthquakes," *Engineering, Technology & Applied Science Research*, vol. 9, no. 6, pp. 5021–5028, Dec. 2019, https://doi.org/10.48084/etasr.3217.

[8] S. Iai and T. Kameoka, "Finite Element Analysis of Earthquake Induced Damage to Anchored Sheet Pile Quay Walls," *Soils and Foundations*, vol. 33, no. 1, pp. 71–91, Mar. 1993, https://doi.org/10.3208/sandf1972.33.71.

[9] S. Tashiro, "Effective Stress Analysis of Quay Walls During the 2011 East Japan Earthquake," in *Developments in Earthquake Geotechnics*, S. Iai, Ed. Cham: Springer International Publishing, 2018, pp. 263–292.

[10] K. Miyashita and T. Nagao, "A Simplified Deformation Estimation Method for Anchor Piles of Sheet Pile Quay Walls under Kinematic Forces during Earthquakes," *Engineering, Technology & Applied Science Research*, vol. 13, no. 1, pp. 10108–10115, Feb. 2023, https://doi.org/10.48084/etasr.5469.

[11] Y. Shiozaki, T. Nagao, O. Ozutsumi, and K. Miyashita, "A Numerical Simulation On The Damaged Example Of Open-Type Wharves On Vertical Piles By The 2-dimentional Effective Stress Analysis," (in Japanese) *Journal of Japan Society of Civil Engineers, Ser. A1 Structural Engineering & Earthquake Engineering*, vol. 65, no. 1, pp. 881-891, Jun. 2009.

[12] T. Nagao and P. Lu, "A simplified reliability estimation method for pile-supported wharf on the residual displacement by earthquake," *Soil Dynamics and Earthquake Engineering*, vol. 129, Feb. 2020, 105904, https://doi.org/10.1016/j.soildyn.2019.105904.

[13] S. Lai, "Seismic analysis and performance of retaining structures," *Geotechnical Earthquake Engineering and Soil Dynamics III*, vol. 75, no. 2, pp. 1020–1044, 1998.

[14] S. Iai, Y. Matsunaga, and T. Kameoka, "Strain Space Plasticity Model for Cyclic Mobility," *Soils and Foundations*, vol. 32, no. 2, pp. 1–15, Jun. 1992, https://doi.org/10.3208/sandf1972.32.2_1.

[15] I. Towhata, "Modeling soil behavior under principal stress axes rotation," *Proc. 5th International Conference on Numerical Methods in Geomechanics, 1985*, vol. 1, pp. 523–530, 1985.

[16] G. Li and R. Motamed, "Finite element modeling of soil-pile response subjected to liquefaction-induced lateral spreading in a large-scale shake table experiment," *Soil Dynamics and Earthquake Engineering*, vol. 92, pp. 573–584, Jan. 2017, https://doi.org/10.1016/j.soildyn.2016.11.001.

[17] P. A. Cundall and O. D. L. Strack, "A discrete numerical model for granular assemblies," *Géotechnique*, vol. 29, no. 1, pp. 47–65, Mar. 1979, https://doi.org/10.1680/geot.1979.29.1.47.

[18] J. Li, B. Wang, P. Pan, H. Chen, D. Wang, and P. Chen, "Failure analysis of soil-rock mixture slopes using coupled MPM-DEM method," *Computers and Geotechnics*, vol. 169, May 2024, Art. no. 106226, https://doi.org/10.1016/j.compgeo.2024.106226.

[19] X. Chen and H. Wang, "Slope Failure of Noncohesive Media Modelled with the Combined Finite–Discrete Element Method," *Applied Sciences*, vol. 9, no. 3, Feb. 2019, Art. no. 579, https://doi.org/10.3390/app9030579.

[20] C. Wu, B. Zhang, and H. Zhang, "Stability Analysis of Coal-Measure Soil Slope Based on Discrete Element Method," *IOP Conference Series: Earth and Environmental Science*, vol. 719, no. 4, Dec. 2021, Art. no. 042059, https://doi.org/10.1088/1755-1315/719/4/042059.

[21] H. Wang, Y. Wang, and F. Jin, "Stability of Expansive Soil Slopes under Wetting–Drying Cycles Based on the Discrete Element Method," *Water*, vol. 16, no. 6, Mar. 2024, Art. no. 861, https://doi.org/10.3390/w16060861.

[22] Q. Liu *et al.*, "Local Scour Mechanism of Offshore Wind Power Pile Foundation Based on CFD-DEM," *Journal of Marine Science and Engineering*, vol. 10, no. 11, Nov. 2022, Art. no. 1724, https://doi.org/10.3390/jmse10111724.

[23] N. Zhang *et al.*, "Numerical Investigation of Local Scour Protection around the Foundation of an Offshore Wind Turbine," *Journal of Marine Science and Engineering*, vol. 12, no. 5, Apr. 2024, Art. no. 692, https://doi.org/10.3390/jmse12050692.

[24] W. Wang, M. Brown, M. Ciantia, and Y. Sharif, "DEM simulation of cyclic tests on an offshore screw pile for floating wind," *Proceedings of the 18th UK Travelling Workshop*, pp. 29–32, Dec. 2021, https://doi.org/10.20933/100001231.

[25] W. Wang, M. J. Brown, M. O. Ciantia, Y. U. Sharif, and B. Cerfontaine, "DEM analysis of helix number effects on offshore screw pile installation and in-service performance," presented at the Proceedings 10th NUMGE 2023, 2023, pp. 1–6, https://doi.org/10.53243/NUMGE2023-217.

[26] B. Cerfontaine, M. O. Ciantia, M. J. Brown, D. J. White, and Y. U. Sharif, "DEM study of particle scale effect on plain and rotary jacked pile behaviour in granular materials," *Computers and Geotechnics*, vol. 161, Sep. 2023, Art. no. 105559, https://doi.org/10.1016/j.compgeo.2023.105559.

[27] S. Yang, M. Zhang, and S. Sang, "DEM Study on the Penetration of Jacked Piles into Layered Soft Clay," *Stavební obzor - Civil Engineering Journal*, vol. 29, no. 3, Oct. 2020, https://doi.org/10.14311/CEJ.2020.03.0033.

[28] J. Feng, R. Luo, X. Dong, X. Zhang, and Q. Shen, "Performance of Monotonic Pile Penetration in Sand: Model Test and DEM Simulation," *Buildings*, vol. 14, no. 10, Oct. 2024, Art. no. 3327, https://doi.org/10.3390/buildings14103327.

[29] Z. Xiao and J. Wang, "DEM in 3D Simulation of Influencing Factors of Deformation Properties and p-y Curves of a Laterally Loaded Pile," in *Computational Science - ICCS 2007, 7th International Conference, Beijing, China, May 27 - 30, 2007, Proceedings, Part III*, 2007, vol. 4489, pp. 1214–1222, https://doi.org/10.1007/978-3-540-72588-6_191.

[30] Y. Xie and T. M. H. Lok, "DEM analysis of ultimate lateral resistance to rigid short piles in sand," *Japanese Geotechnical Society Special Publication*, vol. 2, no. 17, pp. 639–642, 2016, https://doi.org/10.3208/jgssp.TC105-06.

[31] W. Sun and E. Niringiyimana, "DEM Analysis and Prediction for the Lateral Interaction of Monopile in Gravel Soil," *Geotechnical and Geological Engineering*, vol. 38, no. 6, pp. 5955–5967, Dec. 2020, https://doi.org/10.1007/s10706-020-01406-2.

[32] M. Otsubo, C. O'Sullivan, and T. Shire, "Empirical assessment of the critical time increment in explicit particulate discrete element method simulations," *Computers and Geotechnics*, vol. 86, pp. 67–79, Jun. 2017, https://doi.org/10.1016/j.compgeo.2016.12.022.

[33] S. Iai, "Similitude for Shaking Table Tests on Soil-Structure-Fluid Model in 1*g* Gravitational Field," *Soils and Foundations*, vol. 29, no. 1, pp. 105–118, Mar. 1989, https://doi.org/10.3208/sandf1972.29.105.

[34] J. Bauer and O. Reul, "Lateral pressure on pile foundations in cohesive soils due to horizontal soil movements," *Acta Geotechnica*, vol. 19, no. 9, pp. 6375–6390, Apr. 2024, https://doi.org/10.1007/s11440-024-02319-7.

[35] I. Suetomi and N. Yoshida, "Nonlinear Behavior of Surface Deposit During the 1995 Hyogoken-Nambu Earthquake," *Soils and Foundations*, vol. 38, no. Special, pp. 11–22, 1998, https://doi.org/10.3208/sandf.38.Special_11.